AE-OT: A NEW GENERATIVE MODEL BASED ON EXTENDED SEMI-DISCRETE OPTIMAL TRANSPORT

Anonymous authors
Paper under double-blind review

ABSTRACT

Generative adversarial networks (GANs) have attracted huge attention due to its capability to generate visual realistic images. However, most of the existing models suffer from the mode collapse or mode mixture problems. In this work, we give a theoretic explanation of the both problems by Figalli's regularity theory of optimal transportation maps. Basically, the generator compute the transportation maps between the white noise distributions and the data distributions, which are in general discontinuous. However, DNNs can only represent continuous maps. This intrinsic conflict induces mode collapse and mode mixture. In order to tackle the both problems, we explicitly separate the manifold embedding and the optimal transportation; the first part is carried out using an autoencoder to map the images onto the latent space; the second part is accomplished using a GPU-based convex optimization to find the discontinuous transportation maps. Composing the extended OT map and the decoder, we can finally generate new images from the white noise. This AE-OT model avoids representing discontinuous maps by DNNs, therefore effectively prevents mode collapse and mode mixture.

1 INTRODUCTION

GANs (Goodfellow et al. (2014)) emerge as one of the dominant approaches for unconditional image generation. When trained on appropriate data sets, GANs are able to produce realistic and visual appealing samples. GAN methods train an unconditional generator that regresses real images from random noise and a discriminator that measures the difference between generated samples and real images. Despite GANs' advantages, they have critical drawbacks. 1) Training of GANs are tricky and sensitive to hyperparameters. For example, Mescheder et al. (2018) studied 9 different GAN models and variants and showed that gradient descent based optimization is not always locally convergent. 2) GANs suffer from mode collapse, in which the generator only learns to generate few modes of data distribution while missing others, although samples from the missing modes occur throughout the training data (see e.g. Goodfellow (2016)). The phenomenons can be explained as follows:

Manifold Distribution Hypothesis In deep learning, the manifold distribution hypothesis is well accepted, which assumes the distribution of a specific class of natural data is concentrated on a low dimensional manifold embedded in the high dimensional data space Tenenbaum et al. (2000). Therefore, GANs implicitly aim to accomplish two major tasks: 1) manifold embedding: to find the encoding/decoding maps between the data manifold embedded in the image space and the latent space; 2) probability distribution transformation: to transform a given white noise distribution to the data distribution, either in the latent or in the image space.

Distribution Transformation The generator of GAN model is trained to compute a transport map that transforms a known continuous distribution (e.g. Gaussian white noise) to a distribution that aligns well with the empirical real data distribution. Namely, the transport map pushes forward the white noise to a generated distribution to approximate the real data distribution, the similarity between the two distributions determines the generalization ability of the generator Ben-David et al. (2010).

Discontinuity and Mode collapse/Mixture It is a common practice among GAN models that the generators are expressed by deep neural networks, which can only represent continuous functions/mappings. Unfortunately, as pointed out by works Nagarajan & Kolter (2017); Khayatkhoei et al. (2018); Xiao et al. (2018), the transport maps may be discontinuous when there are multiple

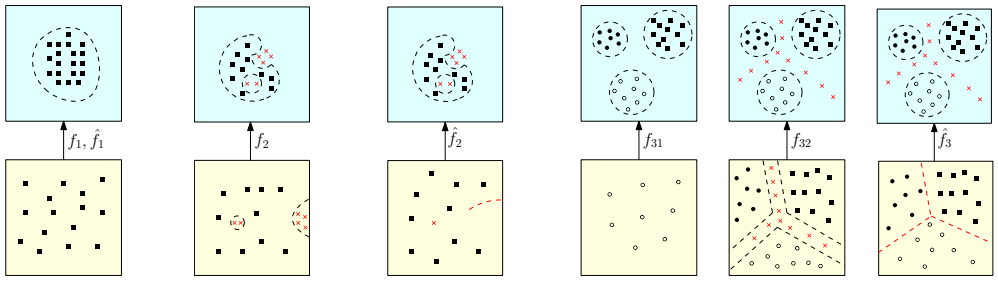

(a) convex support (b) concave support: single mode (c) concave support: multi modes

Figure 1: Mode collapse/mixture caused by the discontinuity of the transport map. Top row shows real data distributions, the bottom row gives the noise distributions. On top, each cluster represents a mode, the spurious generated samples are red crosses (mode mixture); at the bottom, red dotted lines are the singularity set, red crosses are mapped to be spurious samples by DNNs. (a) If the support of the target distribution is convex, DNN (f_1) is able to approximate the transport map $\hat{f}_1$ well. When the support of the target distributions are concave, there are two situations: (b) single mode and (c) multi modes. In (b), DNN, represented by f_2, cannot approximate the transport map $\hat{f}_2$ well and generates some spurious samples. $\hat{f}_3$ gives the transport map of multi-mode, when approximating it with continuous DNNs, either mode collapse f_{31} or mode mixture f_{32} will happen.

modes in the data distribution. This intrinsic conflict can cause mode collapse or mode mixture. The later means that the generated samples mix multiple modes and fall into the gap among the modes. [1]

Currently, we discover a novel phenomena that even the data distribution has a *single mode*, the transport map may still be discontinuous due to the concavity of the support of the data distribution. This can be explained by Brenier's polar factorization theorem Brenier (1991b; 1987; 1991a) and Figalli's regularity theorem Figalli (2010); Chen & Figalli (2017) (Thm. 5 in Appendix B), which asserts that if the support of the target distribution is not convex, then there will be *singularity sets* on the support of the source distribution, such that the transport map is discontinuous on these sets. This shows the intrinsic training difficulty of conventional GANs cannot be eliminated, as shown in Fig. 1.

Conquering Mode Collapse/Mixture However, according to Brenier (1987; 1991a) theorem, the optimal transport map can be represented as the gradient map of the Brenier potential. At the regular points, the Brenier potential is differentiable, its gradient map (the transport map) is continuous; at the singularities, the Brenier potential is continuous but not differentialbe, and its gradient map is discontinuous. Conventional GANs model the gradient map directly and encounter the trouble of discontinuity. In contrast, we propose to model the globally continuous Brenier potential to avoid mode collapse/mixture.

More specifically, our proposed AE-OT model separates the manifold embedding step and the probability distribution transformation step, the former is carried out by an autoencoder (AE), the latter is accomplished by a convex optimization framework (OT). The OT step computes the Brenier potential explicitly and is able to locate the singularity set (the discontinuous points of the gradient map) based on Figalli's theory. Our experimental results demonstrate that the proposed method can not only cover all of the modes, but also avoid generating spurious samples (mode mixture).

Contributions (i) From theoretical aspect, this work gives a thorough explanation of mode collapse and mode mixture by the regularity theory of optimal transportation developed by Figalli (2018 Fields medalist) and the reasons why traditional GANs (DNNS) cannot solve this problem perfectly. (ii) From practical aspect, this work proposes a novel model called AE-OT, which first encodes the data manifold into the latent space, then compute the Brenier potential to represent the optimal transportation map in the latent space. The Figalli's singularity set can be located efficiently and avoided when generating new samples. In this way, our model eliminates mode collapse and mode mixture successfully. (iii) The algorithm for finding the Brenier potential and the optimal transportation map can be accelerated with GPU based convex optimization algorithm. The method converges to the unique global optimum with bounded error estimate. (iv) Our experiment results demonstrate the efficiency and efficacy of the proposed method.

[1] For example, a generator generates obscure digits mixing 0 and 8 but neither 0 nor 8 on the MNIST dataset.

2 RELATED WORK

Optimal Transport Optimal transport plays an important role in various engineering fields. For more thorough reviews, we refer the readers to Peyré & Cuturi (2018) and Solomon (2018). In Gu et al. (2016), the intrinsic connection between Brenier theory in OT and Alexandroff theory in convex geometry was established, and applied for deep learning in Lei et al. (2017) by an convex optimization. Figalli and the collaborators Figalli (2010); Chen & Figalli (2017) proposed that when the support of the data distribution is non-convex, the transport map will be discontinuous.

Generative models In machine learning, generative models have been becoming more important and popular recently. A huge breakthrough for image generating comes from the scheme of Variational Autoencoders (VAEs) (e.g. Kingma & Welling (2013)), where the decoders approximate real data distributions from a Gaussian distribution in a variational approach (e.g Kingma & Welling (2013) and Rezende et al. (2014)). Various recent works followed this scheme, including Adversarial Autoencoders (AAEs) Makhzani et al. (2015) and Wasserstein Autoencoders (WAEs) Tolstikhin et al. (2018). Although VAEs are relatively simple to train, images they generate look blurry. Generative Adversarial Networks (GANs) Goodfellow et al. (2014) were proposed to solve this disadvantage. While being a powerful tool in generating realistically looking samples, GANs can be hard to train and suffer from mode collapsing. Various improvements have been proposed for better training of GANs, including changing the loss function (e.g. Wasserstein GAN Arjovsky et al. (2017)), regularizing the discriminators to be Lipschitz (clipping Arjovsky et al. (2017), gradient regularization Gulrajani et al. (2017), Mescheder et al. (2018) or spectral normalization Miyato et al. (2018)).

Besides, various non-adversarial methods has also been proposed recently. GLO Bojanowski et al. (2017) employs an "encoder-less autoencoder" approach where a generative model is trained with a non-adversarial loss function. IMLE Li & Malik (2018) proposed an ICP related generative model training approach. Later GLANN Hoshen & Malik (2019) combines advantages of GLO and GLANN, where an embedding from image space to latent space was first found using GLO and then a transformation between an arbitrary distribution and latent code was computed using IMLE.

Mitigating Mode Collapsing Recently, Nagarajan & Kolter (2017); Khayatkhoei et al. (2018); Xiao et al. (2018) also realize the training difficulties of GANs come from the approximation of discontinuous functions with continuous DNNs. By the gradient-based regularization, GDGAN Nagarajan & Kolter (2017) do relieve the mode collapse phenomenon of GANs, but mode mixture still exists. Khayatkhoei et al. (2018) proposes to use multiple GANs to overcome the mode collapse. Xiao et al. (2018) proposed to embed the images into a latent space according to Bourgain's theorem, and train the generator by sampling a Gaussian mixture distribution in the latent space instead of a unimodal Gaussian. The recently introduced normalized diversification by Liu et al. (2018) can also help overcome mode collapse successfully. However, all of them cannot solve the mode mixture well.

All these works Nagarajan & Kolter (2017); Khayatkhoei et al. (2018); Xiao et al. (2018) explain that if the target data distribution has multiple modes, the transport map is discontinuous, but DNNs can only represent continuous mappings, the intrinsic conflict causes mode collapse. Our work points out that (i) the approximation of discontinuous OT map by DNNs can not only cause mode collapse, it can also generate samples between modes (mode mixture in multi modes); (ii) even the data distribution has a **single mode**, the transport **map** is **still discontinuous** due to the concavity of its support, hence generation of spurious samples (mode mixture in a single mode) is unavoidable using conventional models. Our work shows that by directly modeling the **continuous Brenier potential**, the mode collapse/mixture can be effectively avoided.

3 COMPUTATIONAL ALGORITHMS

Overview of AE-OT Model Our AE-OT model is summarized in Fig. 2, it has two major components: i) (AE) An autoencoder is trained to encode (f_θ) the data manifold from the image space $\mathcal{X}$ to the latent space $\mathcal{Z}$, and map the data distribution to the latent code distribution; then the decoder g_ξ decodes the latent code back to the data manifold. ii) (OT) This module computes the optimal transportation map T from the noise distribution to the latent code distribution. First, the Brenier potential is found by a convex optimization process according to Gu et al. (2016), whose gradient is the semi-discrete optimal transport map, where the target is the discrete set of latent codes of training samples; then the transport map is piece-wise linearly extended to a global continuous map $\tilde{T}$, where the target becomes a polytope obtained by triangulating the above latent codes. Finally, the

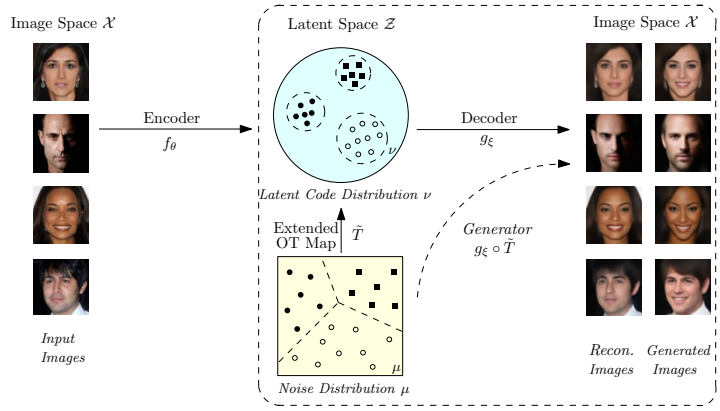

Figure 2: AE-OT model. AE: f_θ and g_ξ represent the encoding and decoding maps respectively, where θ and ξ are their corresponding network parameters. In the latent space $\mathcal{Z}$, the latent codes are clustered into three different modes, represented as marks with different shapes (i.e. disks, squares and circles). OT: The singular set between different modes is plotted with dashed lines. Finally, the generator of our model, which generates realistic images from random noise samples, is the composition of the extended OT map $\tilde{T}$ and the decoding map g_ξ.

singularity set in the source domain is located and avoided when generating new samples. As a result, given a random noise x, we can get the generated image by $g_\xi \circ \tilde{T}(x)$.

Semi-Discrete OT Map Suppose the source measure μ (Gaussian or uniform distribution) is absolutely continuous defined on a convex domain $\Omega \subset \mathbb{R}^d$, the target domain is a discrete set, $Y = \{y_1, y_2, \cdots, y_n\}$, $y_i \in \mathbb{R}^d$, the target measure is a Dirac measure, $\nu = \sum_{i=1}^n \nu_i \delta(y - y_i), i = 1, 2, \ldots, n$, with the equal total mass as the source measure, $\mu(\Omega) = \sum_{i=1}^n \nu_i$. Under a *semi-discrete transport map* $T : \Omega \to Y$, a cell decomposition is induced $\Omega = \bigcup_{i=1}^n W_i$, such that every x in each cell W_i is mapped to the target y_i, $T : x \in W_i \mapsto y_i$. The map T is measure preserving, denoted as $T_{\#}\mu = \nu$, if the μ-volume of each cell W_i equals to the ν-measure of the image $T(W_i) = y_i$, $\mu(W_i) = \nu_i$. The cost function is given by $c : \Omega \times Y \to \mathbb{R}$, where $c(x, y)$ represent the cost for transporting a unit mass from x to y. The total cost of T is given by $\int_\Omega c(x, T(x)) d\mu(x) = \sum_{i=1}^n \int_{W_i} c(x, y_i) d\mu(x)$. *Semi-discrete optimal transport map* is the measure-preserving map that minimizes the total cost, $T^* := \arg\min_{T_{\#}\mu=\nu} \int_\Omega c(x, T(x)) d\mu(x)$.

When the cost function is the L^2 distance $c(x, y) = 1/2\|x - y\|^2$, Brenier's theorem claims that the semi-discrete OT map is given by the gradient map of a PL convex function, the so-called Brenier potential $u_h : \Omega \to \mathbb{R}$, $u_h(x) := \max_{i=1}^n \{\pi_{h,i}(x)\}$, where $\pi_{h,i}(x) = \langle x, y_i \rangle + h_i$ is the hyperplane corresponding to $y_i \in Y$. As shown in Fig. 3(a), the projection of the graph of u_h decomposes Ω into cells $W_i(h)$, each cell $W_i(h)$ is the projection of the supporting plane $\pi_{h,i}(x)$. The height vector h is the unique optimizer of the following convex energy under the condition that $\sum_i h_i = 0$,

$$E(h) = \int_0^h \sum_{i=1}^n w_i(\eta) d\eta_i - \sum_{i=1}^n h_i \nu_i, \tag{1}$$

where $w_i(\eta)$ is the μ-volume of $W_i(\eta)$. The convex energy $E(h)$ can be optimized simply by gradient descend method with $\nabla E(h) = (w_i(h) - \nu_i)^T$.

The key is to compute the μ-volume $w_i(h)$ of each cell $W_i(h)$, which can be estimated using conventional Monte Carlo method. We draw N random samples from μ distribution, $\{x_j\} \sim_{i.i.d.} \mu$, $\forall j \in \mathcal{J}$, the estimated μ-volume of each cell is $\hat{w}_i(h) = \#\{j \in \mathcal{J} \mid x_j \in W_i(h)\}/N$. Given x_j, we can find W_i in which $x_j \in W_i$ by $i = \arg\max_i \{\langle x_j, y_i \rangle + h_i\}, i = 1, 2, \ldots, n$. When N is large enough, $\hat{w}_i(h)$ converges to $w_i(h)$. Then the gradient of the energy is approximated as $\nabla E \approx (\hat{w}_i(h) - \nu_i)^T$. Once the gradient is estimated, we can use Adam algorithm Kingma & Ba (2015) to minimize the energy. Sampling of x is independent of each other and finding the cell that x is located only involves matrix multiplication and sorting. Hence the Monte Carlo method has a natural parallel computation implementation on GPUs.

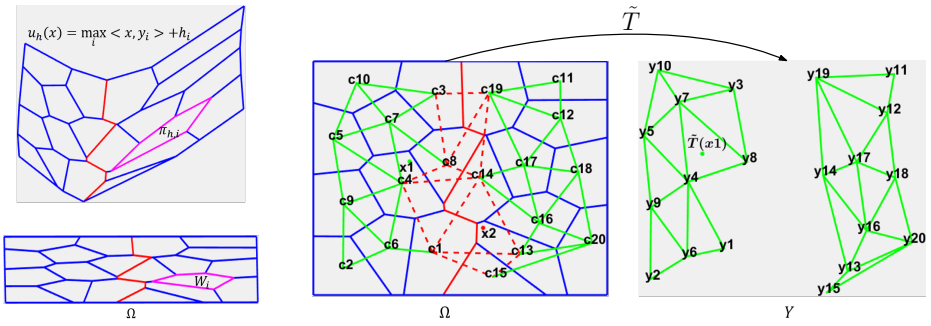

(a) (b)

Figure 3: Illustration of the proposed algorithm with two modes in Y. (a) Brenier potential and the corresponding power diagram. Each cell W_i is mapped to y_i, which is the slope of $\pi_{h,i}$. The red line in Ω gives the singular set. (b) The extended semi-discrete map. By computing the weighted center of each cell, and then triangulating the centers according to the power diagram, we get the PL map $\tilde{T}(x)$ from Ω to Y. If the samples x_1 is not in the triangles transverse the singular set, we map it to the corresponding $\tilde{T}(x_1)$ in Y.

The approximation error is proportional to the inverse of the square root the amount of Monte Carlo samples. Asymptotically the number of Monte Carlo samples increases exponentially with respect to the dimension d (see e.g. Weed & Bach (2017)). This brings huge computational burdens. To find a good balance between precision and speed, we *adaptively* adjust the number of random samples. In practice, we apply the following strategy: if the energy $E(h)$ ceases decreasing for a number of consecutive steps, we double the amount of Monte Carlo samples. The convergence of the proposed algorithm is guaranteed by Kitagawa-Mérigot-Thibert's work (Theorem 1.5 in Kitagawa et al. (2019)). The algorithmic details of semi-discrete OT map are summarized in Alg. 1.

Algorithm 1 Semi-discrete OT Map

Input: Latent codes $Y = \{y_i\}_{i\in\mathcal{I}}$, empirical latent code distribution $\nu = \frac{1}{|\mathcal{I}|}\sum_{i\in\mathcal{I}}\delta_{y_i}$, number of Monte Carlo samples N, positive integer s.
Output: Optimal transport map $T(\cdot)$.
Initialize $h = (h_1, h_2, \ldots, h_{|\mathcal{I}|}) \leftarrow (0, 0, \ldots, 0)$.
repeat
  Generate N uniformly distributed samples $\{x_j\}_{j=1}^N$.
  Calculate $\nabla h = (\hat{w}_i(h) - \nu_i)^T$.
  $\nabla h = \nabla h - mean(\nabla h)$.
  Update h by Adam algorithm with $\beta_1 = 0.9, \beta_2 = 0.5$.
  if $E(h)$ has not decreased for s steps **then**
    $N \leftarrow N \times 2$.
  end if
until Converge
OT map $T(\cdot) \leftarrow \nabla(\max_i\langle\cdot, y_i\rangle + h_i)$.

Algorithm 2 Generate latent code

Input: Optimal transport map $T(\cdot)$, number of samples to generate n, angle threshold $\hat{\theta}$.
Output: Generated latent code P.
Compute $\hat{c}_i$ by Monte Carlo method.
repeat
  Sample $x \sim \mu$, Find the smallest $d+1$ vertex around x as $\{d(x, \hat{c}_{i_0}), d(x, \hat{c}_{i_1}), \ldots, d(x, \hat{c}_{i_d})\}$.
  Compute dihedral angles θ_{i_k} between π_{i_0} and π_{i_k}.
  Select θ_{i_k} with $\theta_{i_k} \le \hat{\theta}$, result in $\hat{i}_k = 0, 1, \ldots, d_1$.
  if $\forall k, \theta_{i_k} > \hat{\theta}$ **then** Abandon x
  else Generate latent code $\tilde{T}(x) = \sum_{k=0}^{d_1}\lambda_k T(\hat{c}_{\hat{i}_k})$ with $\lambda_k = d^{-1}(x, \hat{c}_{\hat{i}_k})/\sum_{j=0}^{d_1} d^{-1}(x, \hat{c}_{\hat{i}_j})$.
  end if
until Generate n new latent code

Piece-wise Linear Extension The semi-discrete OT map $\nabla u_h : \Omega \to Y$ maps all $x \in \Omega$ to the latent codes of training samples $\{y_i\}$'s and won't generate new samples. Therefore, we extend the semi-discrete OT map $T = \nabla u_h$ to a piecewise linear (PL) mapping $\tilde{T}$ as follows. The projection of u_h induces a cell decomposition of Ω, of which each cell is of μ-volume ν_i and is mapped to the corresponding y_i. By representing the cells by their μ-mass centers as $c_i := \int_{W_i(h)} x d\mu(x)$, we can get the point-wise map $t : c_i \mapsto y_i$. The Poincaré of the cell decomposition induces a triangulation of the centers $C = \{c_i\}$: if $W_i \cap W_j \neq \emptyset$, then c_i is connected with c_j to form an edge $[c_i, c_j]$. Similarly, if $W_{i_0} \cap W_{i_1} \cdots \cap W_{i_k} \neq \emptyset$, then there is a k-dimensional simplex $[c_{i_0}, c_{i_1}, \ldots, c_{i_k}]$. All these simplices form a triangulation of C (a simplicial complex), denoted as $\mathcal{T}(C)$ (the green triangles in the left of Fig. 3(b)). We can triangulate Y in the same way to obtain the triangulation $\mathcal{T}(Y)$ (the green triangles in the right of Fig. 3(b)). Once a random sample x is drawn from the distribution μ, we can find the simplex σ in $\mathcal{T}(C)$ containing x. Assume the simplex σ has $d+1$ vertices $\{c_{i_0}, c_{i_1}, \ldots, c_{i_d}\}$, the bary-centric coordinates of x in σ is defined as $x = \sum_{k=0}^d \lambda_k c_{i_k}$, and $\sum_{k=0}^d \lambda_k = 1$ with all λ_k non-negative. Then the generated latent code of x under the PL OT map is given by $\tilde{T}(x) = \sum_{k=0}^d \lambda_k y_{i_k}$ (In Fig. 3(b), the green dot $x1$ is mapped to be $\tilde{T}(x1)$). Because all of the y_is are used to construct the simplicial complex $\mathcal{T}(Y)$ in the support of the target distribution, we can guarantee that no mode is lost.

In practice, the μ-mass center c_i is approximated by the mean value of all the Monte-Carlo samples inside $W_i(h)$, $\hat{c}_i = \sum_{x_j \in W_i} x_j / \#\{x_j \in W_i\}$, where $x_j \sim \mu$. The connectivity information $\mathcal{T}(C)$ is too complicated to construct and to store in high dimensional space, thus $\mathcal{T}(C)$ is not explicitly built. Instead, we find the simplex $\sigma \in \mathcal{T}(C)$ containing x as follows: given a random point $x \in \Omega$, evaluate and sort its Euclidean distances to the centers $d(x, \hat{c}_i), i = 1, 2, \ldots, n$ in the ascending order. Suppose the first $d+1$ items are $\{d(x, \hat{c}_{i_0}), d(x, \hat{c}_{i_1}), \ldots, d(x, \hat{c}_{i_d})\}$, then σ is formed by $\{\hat{c}_{i_k}\}$. The bary-centric coordinates $\hat{\lambda}_{i_k}$ are estimated as $\hat{\lambda}_{i_k} = d^{-1}(x, \hat{c}_{i_k}) / \sum_{k=0}^{d} d^{-1}(x, \hat{c}_{i_k})$. However, this may generate some spurious samples. To overcome it, we need further to detect the singular set.

Singular Set Detection According to Figalli's theory Figalli (2010); Chen & Figalli (2017), if there are multiple modes or the support of the target distribution is concave, there will be singular sets $\Sigma \subset \Omega$, where the Brenier potential is continuous but not differentiable, making its gradient map, i.e. the transport map, discontinuous.

As shown in Fig. 3(a), the source distribution is uniformly defined on Ω, and the target empirical distribution has two modes. There is one ridge (the red line) on the Brenier potential u_h, whose projection is the singular set Σ (the red line in Ω). $\Omega \setminus \Sigma$ consists of two connected components, each of them is mapped onto a single mode. Σ consists of codimension 1 facets of cells. If $W_i(h) \cap W_j(h) \subset \Sigma$, then the dihedral angle between two supporting planes $\pi_{h,i}$ and $\pi_{h,j}$ of u_h is prominently large. Therefore, on the graph of Brenier potential, we pick the pairs of facets whose dihedral angles are larger than a given threshold, the projection of their intersection gives a co-dimension 1 cell in the singular set Σ. During the generation process, if a random sample x is in Σ, we abandon it and draw another sample. This prevents the mode mixture phenomenon.

Given the extended OT map $\tilde{T}(x)$, some of the polyhedrons transverse the singular set (the red lines of Fig .3(b)), which means that different vertices of the polyhedron belongs to different mode. If the sample x falls into such a polyhedron (the dotted red triangle), we just abandon it (as shown in Fig. 3(b), the red dot $x2$ is just abandoned). Specifically, given x, we can detect if it belongs to the singular set by checking the angles θ_{i_k} between π_{i_0} and $\pi_{i_k}, k = 1, 2, \ldots, d$ as $\theta_{i_k} = \langle y_{i_0}, y_{i_k} \rangle / \|y_{i_0}\| \cdot \|y_{i_k}\|$. If all of the angles θ_{i_k} is larger than a threshold $\hat{\theta}$, we say x belongs to the singular set and just abandon it. Or we just select a subset $\{\pi_{i_k}\}$ with $\theta_{i_k} \leq \hat{\theta}$, denoted as $\{\pi_{\hat{i}_k}, k = 0, 1, \ldots, d_1\}$. Then we can compute $\lambda_k = d^{-1}(x, \hat{c}_{\hat{i}_k}) / \sum_{j=0}^{d_1} d^{-1}(x, \hat{c}_{\hat{i}_j})$ and $\tilde{T}(x) = \sum_{k=0}^{d_1} \lambda_k T(\hat{c}_{\hat{i}_k})$. *Intuitively, $\tilde{T}(\cdot)$ smooths the discrete function $T(\cdot)$ in regions where latent codes are dense and keep the discontinuity of $T(\cdot)$ where latent codes are very sparse. In this way we avoid generating spurious latent code and thus improve the generation quality.* The algorithm to generate new code is shown in Alg. 2 and the effect of threshold filtering is further investigated in Appendix C.1.

4 EXPERIMENTS

In order to validate that the proposed method can solve the mode collapse/mixture problems and generate controllable high quality images, several experiments are conducted.

The first experiment focuses on toy sets, so that the complexity of the tasks can be manually controlled and the mode and quality of the generated samples can be accurately computed. Lin et al. (2018) did a large-scale comparison with previous methods that explicitly proposed to mitigate mode collapse and thus established a baseline for comparison. For consistent evaluation, we set up our experiment on the same benchmark dataset as theirs, and make the comparison.

In the second experiment, we run the proposed method mainly on 4 public datasets, MNIST LeCun & Cortes (2010), MNIST-FANSION Han Xiao & Vollgraf (2017), CIFAR-10 Krizhevsky (2009) and CelebA Zhang et al. (2018), just like the authors of Hoshen & Malik (2019) Sajjadi et al. (2018) Lucic et al. (2018) did in their papers. Besides, the architecture of the decoder is the same as Lucic et al. (2018), in which the authors did a large-scale study to evaluated the best performance of 8 different generative models including various GAN models and VAE, and the encoder is set to be the mirror of decoder. The training details, parameter setting and time consuming information are introduced in Section C.5 of the Appendix.

4.1 MITIGATION OF MODE COLLAPSE AND MODE MIXTURE IN SYNTHETIC DATASET

Since synthetic dataset consists of explicit distributions and known modes, mode collapse and the quality of the generated sample can be accurately measured. We choose the same synthetic datasets

Table 1: Experiments on synthetic datasets. Under standard benchmark settings, AE-OT achieves best performances over an average of 10 independent experiment results in terms of modes captured, probability of high quality samples and reverse KL divergence. The mean values and standard deviations of the experiment results are reported here.

	2D-ring			2D-grid		
	Modes (Max 8)	high quality samples	reverse KL	Modes (Max 25)	high quality samples	reverse KL
GAN	6.3±0.5	98.2±0.2%	0.45±0.09	17.3±0.8	94.8±0.7%	0.70±0.07
ALI	6.6±0.3	97.6±0.4%	0.36±0.04	24.1±0.4	95.7±0.6%	0.14±0.03
MD	4.3±0.8	36.6±8.8%	1.93±0.11	23.8±0.5	79.9±3.2%	0.18±0.03
PacGAN2	7.9±0.1	95.6±2.0%	0.07±0.03	23.8±0.7	91.3±0.8%	0.13±0.04
PacGAN3	7.8±0.1	97.7±0.3%	0.10±0.02	24.6±0.4	94.2±0.4%	0.06±0.02
PacGAN4	7.8±0.1	95.9±1.4%	0.07±0.02	24.8±0.2	93.6±0.6%	0.04±0.01
BourGAN	8.0±0.0	99.8±2.9%	4e-4±2e-4	24.9±0.3	95.9±0.2%	0.01±0.02
AE-OT	8.0±0.0	99.6±0.3%	0.004±0.001	25.0±0.0	99.8±0.2%	0.007±0.002

and metrics as in Lin et al. (2018). Specifically, we use 2D-ring and 2D-grid for test sets and *Number of modes*, *Percentage of high-quality samples*, *reverse Kullback-Leibler (KL) divergence* as evaluation metrics. *Number of modes* counts the amount of modes captured by samples produced a generative model. *Percentage of high-quality samples* measures the proportion of samples that generated within three standard deviations of the nearest mode. *reverse KL divergence* measures how well generated samples balance among all modes regarding the real distribution. In Lin et al. (2018), the authors evaluated GAN, ALI, MD and PacGAN on synthetic sets with above three metrics. Each networks are trained under the same generator architecture with a total of approximated 400K training parameters. For AE-OT test, since the source space and the target space are both 2-dimensional, there is no need to train any autoencoder. A two dimensional extended OT map is directly computed. Our results are included in table 1, and benchmarks of previous methods are copied from Lin et al. (2018) and Xiao et al. (2018). Generally speaking, the samples generated by the proposed method can not only cover all of the modes, the quality of them is also better than others. Also, we plot our results on 2D-ring dataset along with those of GAN, PacGAN and BourGAN in Fig. 10 in C.2 of Appendix.

Besides, we experiment on stack MNIST dataset and CelebA dataset to further illustrate the performance of the proposed method, and the results are shown in Section C.3 and C.4 in the Appendix.

4.2 Quantitative comparison with FID

FID is computed by: (1) extract the visual-meaningful features of both the generated and real images through the inception network, (2) fit the features in both the generated and real feature spaces with Gaussian distribution, and then (3) compute the distance between the two Gaussian distributions with the following formula $FID = \|\mu_r - \mu_g\|_2^2 + Tr(\Sigma_r + \Sigma_g - 2(\Sigma_r\Sigma_g)^{\frac{1}{2}})$, where μ_r, μ_g mean the means of the real and generated features, Σ_r, Σ_g represent the variances of both distributions.

We report our results in Tab. (2), in which the compared data comes from Lucic et al. (2018)Hoshen & Malik (2019). In general, the proposed model achieves better than or comparable scores to other state-of-the-art generative models. Theoretically, the FID scores of our proposed generative models should be close to that of the pre-trained autoencoders, and this is also validated in our experiments.

The autoencoder architecture here we use cannot find a good encoding for the CelebA dataset due to the limited capacity. But the FID score of the generation model is still approach to the autoencoder. In order to verify that with appropriate capacity of autoencoder, the proposed model works. We use the generator of DCGAN Radford et al. (2016) as the decoder of the autoencoder, then the reported FID score is 28.6. Also, some of the generated images are displayed in Fig. 12 of the Appendix.

We also display the generating results for the four dataset in Fig. 4. It includes the original images, the results of autoencoders, the best generating results of Lucic et al. (2018), including various GANs and VAE, the results of Hoshen & Malik (2019) and ours, column by column.

Table 2: Quantitative comparison with FID

	Adversarial				Non-Adversarial			Reference	
Dataset	NS GAN	LSGAN	WGAN	BEGAN	VAE	GLO	GLANN	AE	Ours
MNIST	6.8	7.8	6.7	13.1	23.8	49.6	8.6	5.5	**6.4**
Fansion	26.5	30.7	21.5	22.9	58.7	57.7	13.0	4.7	**10.2**
CIFAR-10	58.5	87.1	55.2	71.4	155.7	65.4	46.5	28.2	**38.1**
CelebA	55.0	53.9	41.3	**38.9**	85.7	52.4	46.3	67.5	68.4

Figure 4: The visual comparison of the 4 datasets. The first and second columns provide the real data and the results of autoencoders as comparison. The third column is the generating results from Lucic et al. (2018) with the highest Precision-Recall scores of $(F_8, F_{1/8})$, corresponding to the B dots in Fig. 11; The forth column gives the results of Hoshen & Malik (2019) and the last column shows the results of the proposed method.

Because of the one-one correspondence between μ-mass centers and the images, we show the linear interpolation results (Fig. 13 of Appendix) *between two given images in the dataset*.

Precision and recall proposed in Sajjadi et al. (2018) can compute the precision and the recall at the same time only given the same number of generated and reference images. In Section C.6, we report the comparsion results with state-of-the-art methods.

5 Conclusion

This work gives a theoretic explanation for mode collapse/mixture by Brenier's theory and Figalli's regularity theory of optimal transport maps. When the target measure has concave support, the OT map is discontinuous on the signular sets. But DNNs can only represent continuous functions, this conflict causes the both problems. In order to solve this problem, the AE-OT model is proposed by separating manifold embedding and measure transformation. The former step is computed using an autoencoder, the latter is carried out using the extended semi-discrete OT map based on GPUs. The model is tested thoroughly and extensively by both synthetic and real data sets. The experimental results validates the discontinuity of the OT maps and demonstrate the advantages comparing to the state-of-the-arts.

REFERENCES

Martin Arjovsky, Soumith Chintala, and Léon Bottou. Wasserstein generative adversarial networks. In *ICML*, pp. 214–223, 2017.

Shai Ben-David, John Blitzer, Koby Crammer, Alex Kulesza, Fernando Pereira, and Jennifer Wortman Vaughan. A theory of learning from different domains. *Machine learning*, 79(1-2):151–175, 2010.

Piotr Bojanowski, Armand Joulin, David Lopez-Paz, and Arthur Szlam. Optimizing the latent space of generative networks. *arXiv preprint arXiv:1707.05776*, 2017.

Y. Brenier. Polar decomposition and increasing rearrangement of vector fields. *C. R. Acad. Sci. Paris Sr. I Math.*, 305(19):805–808, 1987.

Y. Brenier. Polar factorization and monotone rearrangement of vector-valued functions. *Comm. Pure Appl. Math.*, 44(4):375–417, 1991a.

Yann Brenier. Polar factorization and monotone rearrangement of vector-valued functions. *Communications on pure and applied mathematics*, 44(4):375–417, 1991b.

L.A. Caffarelli. A localization property of viscosity solutions to the monge-ampére equation and their strict convexity. *Ann. of Math.*, 131(2):129–134, 1990a.

L.A. Caffarelli. Interior w2,p estimates for solutions ofthe monge-ampére equation. *Ann. of Math.*, 131(2):135–150, 1990b.

L.A. Caffarelli. Some regularity properties of solutions of monge ampére equation. *Comm. Pure Appl. Math.*, 44(8-9):965–969, 1991.

Shibing Chen and Alessio Figalli. Partial w2,p regularity for optimal transport maps. *Journal of Functional Analysis*, 272:4588–4605, 2017.

Alessio Figalli. Regularity properties of optimal maps between nonconvex domains in the plane. *Communications in Partial Differential Equations*, 35(3):465–479, February 2010.

Ian Goodfellow. Nips 2016 tutorial: Generative adversarial networks. *arXiv preprint arXiv:1701.00160*, 2016.

Ian Goodfellow, Jean Pouget-Abadie, Mehdi Mirza, Bing Xu, David Warde-Farley, Sherjil Ozair, Aaron Courville, and Yoshua Bengio. Generative adversarial nets. In *NIPS*, pp. 2672–2680, 2014.

David Xianfeng Gu, Feng Luo, jian Sun, and Shing-Tung Yau. Variational principles for minkowski type problems, discrete optimal transport, and discrete monge-ampère equations. *Asian Journal of Mathematics*, 2016.

Ishaan Gulrajani, Faruk Ahmed, Martin Arjovsky, Vincent Dumoulin, and Aaron C Courville. Improved training of wasserstein gans. In *NIPS*, pp. 5769–5779, 2017.

Kashif Rasul Han Xiao and Roland Vollgraf. Fashion-mnist: a novel image dataset for benchmarking machine learning algorithms. *https://arxiv.org/abs/1708.07747*, 2017.

Yedid Hoshen and Jitendra Malik. Non-adversarial image synthesis with generative latent nearest neighbors. In *CVPR*, 2019.

Mahyar Khayatkhoei, Maneesh K. Singh, and Ahmed Elgammal. Disconnected manifold learning for generative adversarial networks. In *Advances in Neural Information Processing Systems*, 2018.

Diederik P Kingma and Jimmy Ba. Adam: A method for stochastic optimization. 2015.

Diederik P Kingma and Max Welling. Auto-encoding variational bayes. *arXiv preprint arXiv:1312.6114*, 2013.

Jun Kitagawa, Quentin Mérigot, and Boris Thibert. Convergence of a newton algorithm for semi-discrete optimal transport. *JOURNAL OF THE EUROPEAN MATHEMATICAL SOCIETY*, 2019.

Alex Krizhevsky. Learning multiple layers of features from tiny images. *Tech report*, 2009.

Yann LeCun and Corinna Cortes. MNIST handwritten digit database. 2010. URL http://yann.lecun.com/exdb/mnist/.

Yann LeCun, Léon Bottou, Yoshua Bengio, and Patrick Haffner. Gradient-based learning applied to document recognition. *Proceedings of the IEEE*, 86(11):2278–2324, 1998.

Na Lei, Kehua Su, Li Cui, Shing-Tung Yau, and David Xianfeng Gu. A geometric view of optimal transportation and generative mode. *Computer Aided Geometric Design*, 2017.

Ke Li and Jitendra Malik. Implicit maximum likelihood estimation. *arXiv preprint arXiv:1809.09087*, 2018.

Zinan Lin, Ashish Khetan, Giulia Fanti, and Sewoong Oh. Pacgan: The power of two samples in generative adversarial networks. In *Advances in Neural Information Processing Systems*, pp. 1505–1514, 2018.

Shaohui Liu, Xiao Zhang, Jianqiao Wangni, and Shi Jianbo. Normalized diversification. In *CVPR*, 2018.

Mario Lucic, Karol Kurach, Marcin Michalski, Sylvain Gelly, and Olivier Bousquet. Are gans created equal? a large-scale study. In *Advances in neural information processing systems*, pp. 698–707, 2018.

Alireza Makhzani, Jonathon Shlens, Navdeep Jaitly, Ian Goodfellow, and Brendan Frey. Adversarial autoencoders. *arXiv preprint arXiv:1511.05644*, 2015.

Lars Mescheder, Andreas Geiger, and Sebastian Nowozin. Which training methods for gans do actually converge? In *ICML*, pp. 3478–3487, 2018.

Takeru Miyato, Toshiki Kataoka, Masanori Koyama, and Yuichi Yoshida. Spectral normalization for generative adversarial networks. In *ICLR*, 2018.

Vaishnavh Nagarajan and J. Zico Kolter. Gradient descent gan optimization is locally stable. In *Advances in Neural Information Processing Systems*, 2017.

Gabriel Peyré and Marco Cuturi. *Computational Optimal Transport*. https://arxiv.org/abs/1803.00567, 2018.

Alec Radford, Luke Metz, and Soumith Chintala. Unsupervised representation learning with deep convolutional generative adversarial networks. In *ICLR*, 2016.

Danilo Jimenez Rezende, Shakir Mohamed, and Daan Wierstra. Stochastic backpropagation and approximate inference in deep generative models. *arXiv preprint arXiv:1401.4082*, 2014.

Mehdi SM Sajjadi, Olivier Bachem, Mario Lucic, Olivier Bousquet, and Sylvain Gelly. Assessing generative models via precision and recall. *arXiv preprint arXiv:1806.00035*, 2018.

Tim Salimans, Ian Goodfellow, Wojciech Zaremba, Vicki Cheung, Alec Radford, and Xi Chen. Improved techniques for training gans. In *NIPS*, pp. 2234–2242, 2016.

Justin Solomon. *Optimal Transport on Discrete Domains*. https://arxiv.org/abs/1801.07745, 2018.

J B Tenenbaum, V Silva, and J C Langford. A global geometric framework for nonlinear dimensionality reduction. *Science*, 290(5500):2391–232, 2000.

Ilya Tolstikhin, Olivier Bousquet, Sylvain Gelly, and Bernhard Schoelkopf. Wasserstein auto-encoders. In *ICLR*, 2018.

Cédric Villani. *Optimal transport: old and new*, volume 338. Springer Science & Business Media, 2008.

Jonathan Weed and Francis Bach. Sharp asymptotic and finite-sample rates of convergence of empirical measures in wasserstein distance. *arXiv preprint arXiv:1707.00087*, 2017.

Chang Xiao, Peilin Zhong, and Changxi Zheng. Bourgan: Generative networks with metric embeddings. In *Advances in Neural Information Processing Systems*, 2018.

Zhanpeng Zhang, Ping Luo, Chen Change Loy, and Xiaoou Tang. From facial expression recognition to interpersonal relation prediction. *International Journal of Computer Vision*, 2018.

A BRENIER'S THEORY

In this subsection, we briefly introduce the basic concepts and theorems in optimal transport theory, which comes from Brenier theory Villani (2008); Brenier (1987; 1991a), and discrete theory Gu et al. (2016).

Optimal transport Problem Suppose $X, Y \subset \mathbb{R}^d$ are two subsets of n-dimensional Euclidean space, μ, ν are two probability measured defined on X and Y respectively, with equal total measure, $\mu(X) = \nu(Y)$. A map $T : X \to Y$ is *measure preserving*, denoted as $T_{\#}\mu = \nu$, if for any measurable set $B \subset Y$, $\mu(T^{-1}(B)) = \nu(B)$. Given a cost function $c(x, y) : X \times Y \to \mathbb{R}_{\geq 0}$, indicating the cost of moving each unit mass from the source to the target, the total *transport cost* of the map T is defined to be $\int_X c(x, T(x))d\mu(x)$.

The *Monge's problem* of optimal transport arises from finding the measure-preserving map that minimizes the total transport cost.

$$(MP) \quad \mathcal{W}_c(\mu, \nu) := \min_{T_{\#}\mu=\nu} \int_X c(x, T(x))d\mu(x). \tag{2}$$

The solutions to the Monge's problem is called the *optimal transport map*, whose total transport cost is called the *Wasserstein distance* between μ and ν, denoted as $\mathcal{W}_c(\mu, \nu)$.

Brenier's Approach Brenier Brenier (1987; 1991a) proved the following theorem:

Theorem 1 (Brenier Brenier (1987; 1991b))**.** *Suppose X and Y are the Euclidean space $\mathbb{R}^d$ and the transport cost is the quadratic Euclidean distance $c(x, y) = 1/2\|x - y\|^2$. Furthermore μ is absolutely continuous and μ and ν have finite second order moments, then there exists a convex function $u : X \to \mathbb{R}$, the so-called Briener potential, its gradient map ∇u gives the solution to the Monge's problem. The Brenier potential is unique up to a constant.*

Brenier's polar factorization theorem claims that: for any measure preserving map $T_{\#}\mu = \nu$, T can be uniquely decomposes into the forms $T = \nabla u \circ s$, where $s : X \to X$ is a volume preserving map and ∇u is the optimal transport map under L^2 cost. Therefore, the regularity of T can be determined by that of ∇u.

Discrete Brenier's Theorem Brenier theorem can be directly generalized to discrete target measure. Suppose the source measure μ is defined on a compact convex set Ω, the target measure $\nu = \sum_{i=1}^n \nu_i \delta(y - y_i)$, $\mu(\Omega) = \sum_i \nu_i$. The discrete Brenier potential is a piecewise linear function,

$$u_h(x) = \max_{i=1}^n \{\pi_{h,i}(x)\} = \max_{i=1}^n \{\langle x, y_i \rangle + h_i\}. \tag{3}$$

As shown in Fig. 3(a), the projection of the Brenier potential induces a cell decomposition of Ω, each cell $W_i(h) := \{p \in \Omega | \nabla u_h(p) = y_i\}$, whose μ-measure is denoted as $w_i(h)$.

Theorem 2 (Discrete Brenier Theorem Gu et al. (2016))**.** *For any $\nu_1, \nu_2, \ldots, \nu_n > 0$ with $\sum_{i=1}^n \nu_i = \mu(\Omega)$, there exists $h = (h_1, h_2, \ldots, h_n) \in \mathbb{R}^n$, unique up to adding a constant $(c, c, \ldots, c)$, so that $w_i(h) = \nu_i$, for all i. The vector h is the unique minimum argument of the following convex energy*

$$E(h) = \int_0^h \sum_{i=1}^n w_i(\eta)d\eta_i - \sum_{i=1}^n h_i \nu_i, \tag{4}$$

defined on an open convex set $\mathcal{H} = \{h \in \mathbb{R}^n : w_i(h) > 0, i = 1, 2, \ldots, n\}$. Furthermore, ∇u_h minimizes the quadratic cost $\int_\Omega \|x - T(x)\|^2 d\mu(x)$ among all transport maps $T_{\#}\mu = \nu$. The gradient of above energy is given by $\nabla E(h) = (w_1(h) - \nu_1, w_2(h) - \nu_2, \ldots, w_n(h) - \nu_n)^T$. The Hessian of the energy is given by

$$\frac{\partial w_i}{\partial h_j} = -\frac{\mu(W_i \cap W_j)}{\|y_i - y_j\|}, \frac{\partial w_i}{\partial h_i} = \sum_{j \neq i} \frac{\partial w_i}{\partial h_j}. \tag{5}$$

The optimal transport map can be obtained by convex optimization. Furthermore, the optimization can be carried out using Newton's method. The global linear convergence rate is guaranteed by the following theorem:

Theorem 3 (Kitagawa-Mérigot-Thibert Kitagawa et al. (2019))**.** *Assume the cost function is quadratic distance, μ has convex support and also that (i) The probability density of μ is $C^{0,\alpha}(\Omega)$ for α in $(0; 1]$. (ii) μ has positive Poincaré-Wirtinger constant. Then the Newton algorithm for semi-discrete optimal transport converges globally with linear rate and locally with rate $1 + \alpha$.*

The gradient descend method is applied in GPU, this theorem ensures the convergence.

B FIGALLI'S THEORY

In this section, we show the fact that even for the case of **single mode**, the transport map may still be **discontinuous**, which will cause the instability of the training process of GANs. The arguments are mainly based on the regularity theory of transport maps developed by Figalli Chen & Figalli (2017); Figalli (2010) and so on.

According to Brenier's Theorem Brenier (1987; 1991a), any transport map can be decomposed into a measure preserving map and a solution to the Monge-Ampére equation, which is the optimal transport map under the L^2 cost function. Therefore, the continuity of the transport map can be reduced to the regularity (smoothness) of the solution to the Monge-Ampére equation. When the support of the target measure is convex and the density functions are smooth, Caffarelli showed the map is differentiable; otherwise if the target domain is not convex, Figalli showed the map is discontinuous, and gave precise description of the singularity set. In this section, we briefly introduce Figallis' theory, and conduct an experiment using CelebA data set to show the existence of the singularity set, hence demonstrate the fact that the transport maps computed in GANs are discontinuous.

B.1 CONVEX DOMAINS - CAFFARELLI THEOREM

Let Ω and Λ are two bounded open sets in $\mathbb{R}^n$, and let $f : \mathbb{R}^n \to \mathbb{R}$ and $g : \mathbb{R}^n \to \mathbb{R}$ be two positive functions such that $f = 0$ in $\mathbb{R}^n \setminus \Omega$, $g = 0$ in $\mathbb{R}^n \setminus \Lambda$, and

$$\int_\Omega f = \int_\Lambda g = 1.$$

According to Brenier's Theorem Brenier (1987; 1991a), there exists a globally Lipschitz convex function $\varphi : \mathbb{R}^n \to \mathbb{R}$ such that $\nabla\varphi_\# f = g$ and and $\nabla\varphi(x) \in \bar{\Lambda}$ for $\mathcal{L}^2$-a.e. $x \in \mathbb{R}^n$. We say φ weakly solves the Monge-Ampére equation

$$det(D^2\varphi) = \frac{f}{g \circ \nabla\varphi} \quad in\ \mathbb{R}^n, \tag{6}$$

together with the boundary condition $\nabla\varphi(\mathbb{R}^n) \subset \bar{\Lambda}$. φ is called the *Briener potential*.

As shown by Caffarelli [9], if Λ is convex, then φ is strictly convex, and it solves the Monge-Ampére equation 6. The regularity theory has been estabilished (see Caffarelli (1990a;b; 1991)), such as

1. if $\lambda \le f, g \le 1/\lambda$ for some $\lambda > 0$, then $\varphi \in C^{1,\alpha(\lambda)}_{loc}(\Omega)$.
2. if $f \in C^{k,\alpha}_{loc}(\Omega)$ and $g \in C^{k,\alpha}_{loc}(\Lambda)$, then $\varphi \in C^{k+2,\alpha}_{loc}(\Omega)$, $(k \ge 0, \alpha \in (0, 1))$.

B.2 NON-CONVEX DOMAINS - FIGALLI THEOREM

However, if Λ is not convex, the regularity of the Brenier potential can not be guaranteed. For example one can find an example, such that

1. Ω is convex, Λ is simply connected, but non-convex;
2. the density functions f and g are smooth, $f \in C^\infty(\Omega)$ and $g \in C^\infty(\Lambda)$;
3. the Brenier potential $\varphi \notin C^1(\Omega)$, the transport map $\nabla\varphi$ is not continuous.

In this scenario, the transport map can not be learned using DNNs, and training process is unstable or the GAN model generates unrealistic samples.

Figalli's construction Let $\varphi : \mathbb{R}^n \to \mathbb{R}$ be a convex function. Its *subdifferential* at a point x is defined by

$$\partial\varphi(x) := \{y \in \mathbb{R}^n | \varphi(z) \geq \varphi(x) + y \cdot (z - x), \forall z \in \mathbb{R}^n\}.$$

φ is differentiable at a point x if and only if $\partial\varphi(x)$ is a singleton. Figalli decomposes the set of non-differentiability points according to the dimension of the singular set:

$$\Sigma_k(\varphi) := \{x \in \mathbb{R}^n | dim(\partial\varphi) = k\}, k = 0, \ldots, n. \tag{7}$$

For any $k = 0, \ldots, n$, the set $\Sigma_k(\varphi)$ is $(n-k)$-rectifiable. The set of *reachable subgradients* at x as

$$\nabla_*\varphi := \left\{ \lim_{k \to +\infty} \nabla\varphi(x_k) | x_k \in \Sigma_0, x_k \to x \right\}.$$

It is known that the convex hull of $\nabla_*\varphi(x)$, coincides with $\partial\varphi(x)$.

Theorem 4 (Figalli)**.** *Assume that there exists $\lambda > 0$ such that $\lambda \leq f \leq 1/\lambda$ in Ω, $\lambda \leq g \leq 1/\lambda$ in Λ, and that $\partial\Omega$ and $\partial\Lambda$ are continuous. Then φ is strictly convex inside Ω. Moreover there exist two open sets $\Omega' \subset \Omega$ and $\Lambda' \subset \Lambda$, with $\mathcal{L}^2(\Omega \setminus \Omega') = \mathcal{L}^2(\Lambda \setminus \Lambda') = 0$, such that $\varphi \in C^{1,\alpha}(\Omega')$, $\nabla\varphi$ is a bi-Hölder homeomorphism between Ω' and Λ', and φ is an Alexandrov solution of 6 inside Ω'. In particular, Caffarelli's regularity theory for strictly convex Alexandrov solutions of the Monge-Ampére equations applies to φ inside Ω'.*

Figalli studies the singular set of φ in Ω, i.e. the set of points $x \in \Omega$ where φ is not differentiable, denoted as $Sing$. Figalli shows the singularity set has the following characterization,

$$Sing = \{x \in \Omega | \partial\varphi(x) \cap \Lambda = \emptyset, \nabla_*\varphi(x) \subset \partial\Lambda, \partial\varphi(x) \not\subset \Lambda\}.$$

it can be decomposed into connected components $Sing := \cup_i S_i$. For planar case,

Theorem 5 (Figalli Singularity Set)**.** *The number of connected components of $Sing$ is at most countable. Moreover:*

1. *either S_i coincides with an isolated point $\{xi\}$ for some $x_i \in \Omega$, and in this case the boundary of $\partial(xi)$ is entirely contained inside $\partial\Lambda$ (so that $\partial\varphi(xi)$ completely fills a hole in Λ);*
2. *or S_i can be written as a disjoint union as follows:*

$$S_i = \bigcup_j \gamma_{ij},$$

where $\gamma_{ij} : I_{ij} \to Sing$ are embedded Lipschitz curves parameterized by arc-lengh, I_{ij} is an interval.

B.3 Elementary Experiments

We have designed several numerical experiments to verify Figalli's theorems in low dimensional cases.

As shown in Fig. 5, the source domain Ω is a rectangle, the target domain Λ is a dumb-cell shape, the density functions f and g are constant 1, namely, uniform distribution. The optimal transport maps is obtained using our method, the Brenier potential φ is not differentiable, the singularity set is near the middle of the rectangle, $\Sigma_1(\varphi) = \gamma_1 \cup \gamma_2$ as shown in the figure. At γ_1 and γ_2, φ is continuous but not differentiable. Each point $x \in \Omega$ is mapped onto $\nabla\varphi(x) \in \Lambda$ with the same color. This shows even the target domain is simply connected, the concavity will induce the discontinuity of the transport map.

Fig. 6 shows another computational result, which demonstrates the singularity structure in Figalli's theorem. The source domain Ω is the unit disk, the target domain Λ is with complicated geometry. The singularity set of the optimal transport map satisfies the description of Figalli's theorem 4,

$$\Sigma_1 = \bigcup_{i=0}^{3} \gamma_k, \ \Sigma_2 = \bigcup_{j=0}^{1} x_j.$$

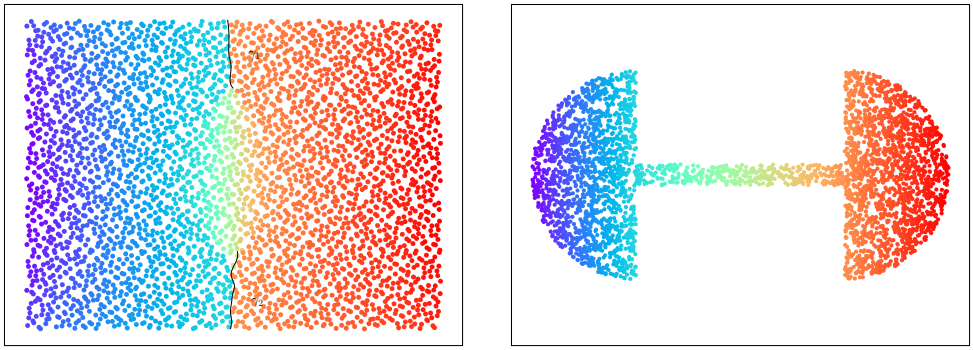

Figure 5: Discontinuous Optimal transport map, γ_1 and γ_2 are two singularity sets.

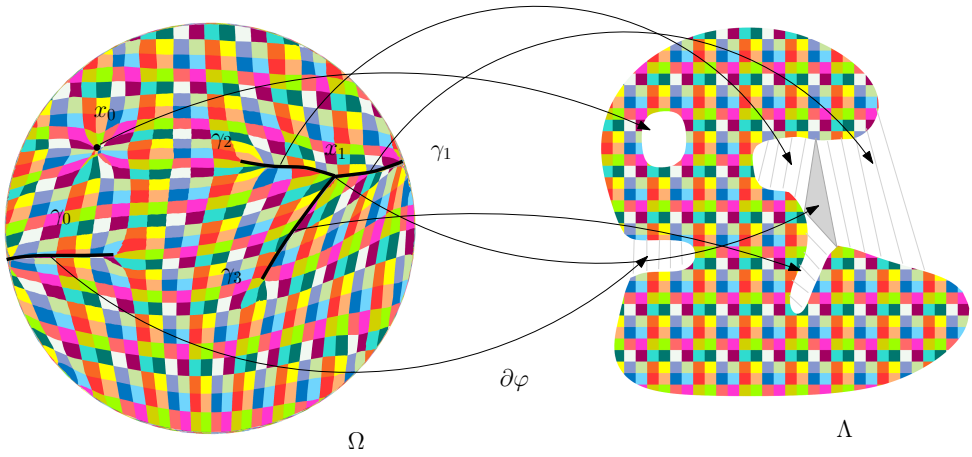

Figure 6: Singularity structure of an optimal transport map.

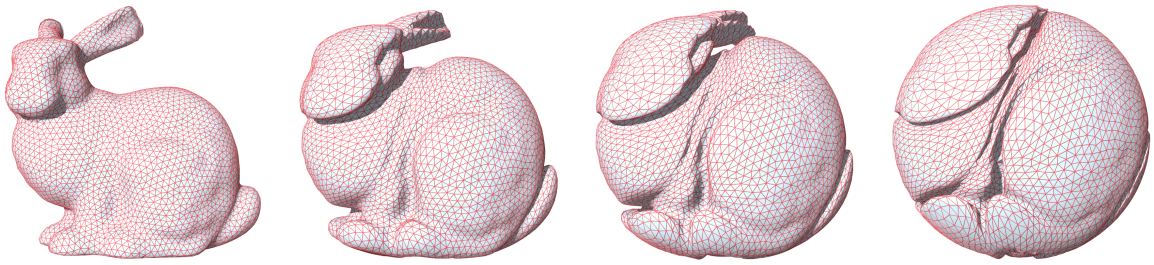

Figure 7: Optimal transport between a solid ball to the Stanford bunny. The singular sets are the foldings on the boundary surface.

$\partial\varphi(x_0)$ fills the hole on Λ. For any interior point $p \in \gamma_1$, $\partial\varphi(p)$ is a line segment connecting two points on the boundary of Λ.

Fig. 7 shows the singularity set of an optimal transport map between volumetric domains. Ω is the solid ball, Γ is the interior of Stanford bunny. The probability distributions are the uniform distribution. The Brenier potential φ is obtained by solving the Monge-Ampére equation. The optimal transport map is visualized by a morphing sequence: $f_t := (1-t)id + t\nabla\varphi$ for $0 \leq t \leq 1$, the intermediate shape is given by $f_t(\Lambda)$. It is obvious that the boundary surface of the bunny is folded inside the ball, which form the singularity set of the optimal transport map $\nabla\varphi$.

B.4 EXPERIMENTS ON REAL DATA SETS

The low dimensional experiments demonstrates Figalli's theorems, which are general for any dimension. In the following, we design and carry out an experiment for high dimensional real data, CelebA.

(a) generated facial images (b) a path through a singularity.

Figure 8: Facial images generated by an AE-OT model, the image in the center of (b) shows the transport map is discontinuous.

As shown in Fig. 8, we use an Autoencoder to encode the CelebA data samples to the latent space, which can be treated as a probability distribution with density function $g : \Lambda \to \mathbb{R}$, whose support set is Λ. We define the source domain Ω as the unit cube, the source density function $f \equiv 1$, namely uniform distribution. Then we compute the optimal transport map from (Ω, f) to (Λ, g), the Briener potential is φ. Then we random generate a sample x from (Ω, f), then map it to the data distribution (Λ, g), the image is $\nabla\varphi(x)$. Finally, $\nabla\varphi(x)$ is mapped back to the image space by the decoder map to obtain a generated facial image. Fig. 8 left frame shows the examples of generated facial images.

We then search the evidence of the existence of the singularity set of the Brenier potential φ. We randomly draw a line segment, γ, which produce morphing sequence between two facial images as shown in the right frame of Fig. 8. The starting point $\gamma(0)$ corresponds to the boy face with brown eyes on the left top corner, the ending point $\gamma(1)$ represents the girl face with blue eyes on the right bottom corner. For each $t \in [0, 1]$, $\gamma(t)$ is mapped by $\nabla\varphi$ to the latent data distribution (Λ, g), then decoded to an facial image interpolating the boy and the girl facial images.

In the center of frame (b), for some specific $t_0 \in (0, 1)$, the generated image by $\gamma(t_0)$ is with one blue eye and one brown eye. In reality, such kind of persons are extremely rare, therefore, we can treat such kind of facial images as on the boundary of the support Λ of the data distribution g in the latent space. This means t_0 is in the singularity set of φ, the subgradient $\partial\varphi(\gamma(t_0))$ intersects $\partial\Lambda$ at multiple points. The Brenier potential at $\gamma(t_0)$ is only continuous but not differentiable, $\nabla\varphi$ at $\gamma(t_0)$ is discontinuous.

In summary, the generated unrealistic facial image shows the transport map is discontinuous, which verifies our hypothesis: the concavity of the support of the real data distribution causes the discontinuity of the transport map, which can not be directly represented by DNNs and induces instability of the training process or generating unrealistic samples.

C ADDITIONAL EXPERIMENTS

C.1 SINGLE PARAMETER SELECTIVE INTERPOLATION

On synthetic datasets, effects of angle threshold filtering can be visually inspected. As illustrated in Fig. 9, number of mode is a monotonically increasing function with respect to angle threshold $\hat{\theta}$. Quality of generated samples is effected directly by choosing different $\hat{\theta}$. Generally, small $\hat{\theta}$ encourages interpolation in between closely related real samples while too large $\hat{\theta}$ will result in interpolation between samples from different modes, which might in turn lower generation quality. On synthetic datasets, where modes are isotropic and different modes are clearly separable, an ideal $\hat{\theta}$ that captures all modes while avoids generating low quality samples can be chosen within a relatively wide band. For real world datasets of unknown modes, an ideal $\hat{\theta}$ needs to be hand tuned as the separability of different modes depends largely on input data pattern and quality of the embedding map.

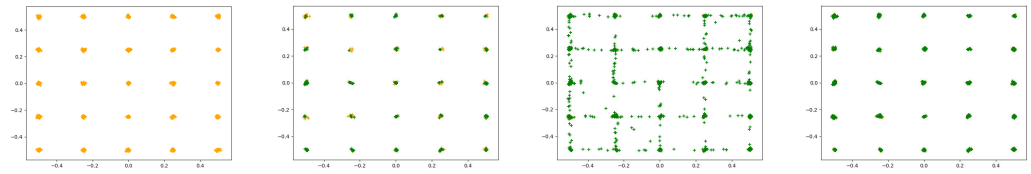

(a) Target Distribution (b) $\hat{\theta}$ too small (c) $\hat{\theta}$ too large (d) Proper $\hat{\theta}$

Figure 9: Effect of increasing angle threshold $\hat{\theta}$. (a) shows target distribution. (b) and (c) shows AE-OT results when $\hat{\theta}$ is too small (as in (b)) or too large (as in (c)). (d) shows a proper choice of $\hat{\theta}$ that precisely captured and generalized all modes.

C.2 MORE RESULTS IN SYNTHETIC DATASETS

For illustration purpose, we plot our results on 2D-ring dataset along with those of GAN, PacGAN and BourGAN in Fig. 10. It is obvious that our method not only covers all of the modes, also the generation of meaningless data is overcome.

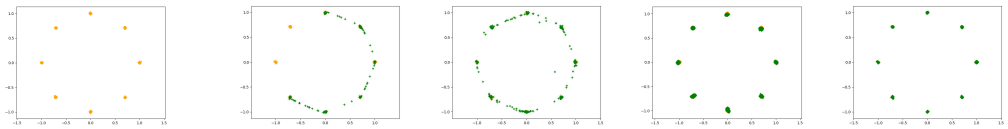

(a) Target Distribution (b) GAN (c) PacGAN BourGAN (d) AE-OT

Figure 10: Experiments results on synthetic datasets. The generation of 8 Gaussians in 2D-circle by GAN, PACGAN. BourGAN and AE-OT. (a) Target Distribution. (b) Generated samples of GAN model. (c) Generated samples of PacGAN. (d) Generated samples of BourGAN (e) Generated samples of AE-OT. It is observed that samples generated by the GAN model fail to capture all modes. Samples from PacGAN capture all modes, but with inter-mode spurious samples. Though both BourGAN and AE-OT capture the target multimodal distribution precisely, the generation quality of the proposed method is better than BourGAN.

C.3 STACK MNIST EXPERIMENT

Experiments of varisou GAN models on stacked MNIST dataset are in consistent with Lin et al. (2018). For AE-OT model, we use the architecture shown in table 3 and table 4, with the decoder architecture same as the consistent generator architectures in GANs, and encoder having mirrored architecture.

Table 3: Encoder architecture for stack MNIST

layer	number of outputs	kernel size	stride	BN	activation
Input $x \sim P_{data}$	28*28*3				
Convolution	14*14*16	5*5	2		LeakyReLU
Convolution	7*7*32	5*5	2	Yes	LeakyReLU
Convolution	4*4*64	5*5	2	Yes	LeakyReLU
Convolution	2*2*128	5*5	2	Yes	LeakyReLU
Fully connected	100				

Table 4: Decoder architecture for stack MNIST

layer	number of outputs	kernel size	stride	BN	activation
Input $z \sim P_{latent}$	100				
Fully connected	2*2*128			Yes	ReLU
Transposed Convolution	4*4*64	5*5	2	Yes	ReLU
Transposed Convolution	7*7*32	5*5	2	Yes	ReLU
Transposed Convolution	14*14*16	5*5	2	Yes	ReLU
Transposed Convolution	28*28*3	5*5	2		Tanh

We test diversity of generated samples from our AE-OT method on stack MNIST dataset that consists of 128,000 samples in 1,000 modes with each sample stacking three handwritten digit images from MNIST dataset LeCun et al. (1998). *Number of modes* counts the amount of modes captured by samples produced a generative model. The *reverse KL divergence* is computed by first assign each samples to their nearest mode, and compute the KL divergence between histogram of sample count on each mode and the histogram of real data. We choose angle threshold $\hat{\theta} = 0.5$ for AE-OT method. Details of network architectures are listed in supplementary materials. Experiments results are summarized in table 5, which show our method achieves best performance in terms of modes captured and reverse KL divergence on stacked MNIST dataset.

Table 5: Experiments on stacked MNIST. Results have shown that our method achieves best results in terms of mode captured and reverse KL divergence. (*) In WGAN, PacWGAN and AE-OT experiments, number of feature maps in each network layer is a quarter of those in other experiments.

	Stacked MNIST	
	Modes	KL
DCGAN	99.0	3.40
ALI	16.0	5.40
Unrolled GAN	48.7	4.32
VEEGAN	150.0	2.95
MD	24.5 ± 7.67	5.49 ± 0.42
PacDCGAN4	1000.0 ± 0.00	0.07 ± 0.005
WGAN(*)	314.3 ± 38.54	2.44 ± 0.170
PacWGAN4(*)	965.7 ± 19.07	0.42 ± 0.094
AE-OT(*)	$\mathbf{1000.0 \pm 0.0}$	$\mathbf{0.03 \pm 0.0008}$

C.4 CelebA Experiment

we evaluate our method on CelebA dataset by measuring collision probability in a batch of 1024 generated images of size 64-by-64. If a pair of identical images appear, a collision is declared, and thus higher collision probability means lower generation diversity. The same metric has been used in Lin et al. (2018) for evaluation of PacGAN. To make a consistent comparison, we design our autoencoder network with encoder having the same architecture as in previous work and decoder having a mirrored architecture of encoder. Angle threshold $\hat{\theta}$ is chosen to be 0.7 for AE-OT test. Results are listed in table 6, with corresponding images can be downloaded here. Results have

shown that our method achieves best result in terms of probability of collision. Autoencoder network structures can be found at table 7 and 8.

Table 6: Probability of identical images in a batch of 1024 generated images from DCGAN, PacGAN2 and AE-OT. Results have shown that our method achives best result in terms of collision probability on CelebA dataset.

Discriminator size	Probability of collision		
(Decoder size)	DCGAN	PacDCGAN2	AE-OT
273K	1	0.33	**0**
4×273K	0.42	0	**0**
16×273K	0.86	0	**0**
25×273K	0.65	0.17	**0**

Table 7: Encoder architecture in CelebA experiment

layer	number of outputs	kernel size	stride	BN	activation
Input $x \sim P_{data}$	64*64*3				
Convolution	32*32*dim_f	4*4	2		LeakyReLU
Convolution	16*16*dim_f*2	4*4	2	Yes	LeakyReLU
Convolution	8*8*dim_f*4	4*4	2	Yes	LeakyReLU
Convolution	4*4*dim_f*8	4*4	2	Yes	LeakyReLU
Convolution	100	4*4	1		

Table 8: Decoder architecture in CelebA experiment

layer	number of outputs	kernel size	stride	BN	activation
Input $z \sim P_{latent}$	100				
Transposed Convolution	4*4*dim_f*8				
Transposed Convolution	8*8*dim_f*4	4*4	2	Yes	ReLU
Transposed Convolution	16*16*dim_f*2	4*4	2	Yes	ReLU
Transposed Convolution	32*32*dim_f	4*4	2	Yes	ReLU
Transposed Convolution	64*64*3	4*4	2		Tanh

C.5 Parameter Setting and Training Details of AE-OT on 4 Public Datasets

During the training of the autoencoders for MNIST, FANSION, Cifar10 and CelebA, when the L_2 loss stops descending, which means that the network has found a good encoding function of the image space, we freeze the encoder part and continue to train the network from latent space to image space. And for the autoencoders, we run 200 epochs in total, including 150 epochs before the freezing of decoder, and 50 epochs after. The training loss before and after the freezing of decoder is shown in Tab. 9.

Besides, the parameters involved in the OT computation is set as follows: we set the parameters of Adam algorithm to be $\alpha = 1.0, \beta_1 = 0.9, \beta_2 = 0.5$ for all the experiments. The $\hat{\theta}$ is different for different tasks. Specifically, for the MNIST and the FANSION-MNIST dataset, $\hat{\theta} = \arccos 0.8$; for CIFAR10 and CelebA, $\hat{\theta} = \arccos 0.65$. When the sum of measure difference $\sum_{i=1}^{N} |\hat{w}_i(h) - \nu_i|$ is less than 0.05, the loops stop.

The time consumed by AE-OT is mainly composed of two parts: the training of autoencoder and the computation of semi-discrete OT. The training details of the former is illustrated in Section C.5 of the Appendix and we report the latter in table 10 with the Intel Core i7-7820X CPU and NVIDIA GTX1080Ti GPU. Here the dimension of the latent code is 64 for all of the four datasets.

Table 9: The L_2 loss of the autoencoders before and after the freezing of encoder

	MNIST	FANSION	CIFAR-10	CelebA
Before	0.0013	0.0026	0.0023	0.0077
After	0.0005	0.0011	0.0018	0.0074

Table 10: Time used to compute the semi-discrete OT for the four datasets.

MNIST		FANSION		CIFAR10		CelebA	
Num	Time(min)	Num	Time(min)	Num	Time(min)	Num	Time(min)
60k	$\sim$120	60k	$\sim$120	50k	$\sim$95	$\sim$190k	$\sim$480

C.6 Quantitative comparison with precision and recall

FID score is an effective method to test the difference between the generated distribution and real data, but it mainly focuses on precision, and cannot accurately capture how much portion of real data a generative model could cover. The method proposed in Sajjadi et al. (2018) can compute the precision and the recall at the same time only given the same number of generated and reference images. Firstly, the images are encoded to the feature space by the inception netSalimans et al. (2016). Secondly, the features corresponding to generated and real data were put together and clustered. Thirdly, the histograms, marked as $P(\omega)$ and $Q(\omega)$ for the both kinds of images appeared in each cluster are computed. Finally, the precision $\alpha(\lambda)$ and recall $\beta(\lambda)$ can be defined as follows:

$$\alpha(\lambda) = \sum_{\omega \in \Omega} min(\lambda P(\omega), Q(\omega)) \tag{8}$$

$$\beta(\lambda) = \sum_{\omega \in \Omega} min(P(\omega), \frac{Q(\omega)}{\lambda}) \tag{9}$$

With different λ, we can get different pairs of $(\alpha(\lambda), \beta(\lambda))$. After the above definition, we can used the concept of $(F_8, F_{1/8})$ defined on Sajjadi et al. (2018) to quantify the relative importance of precision and recall.

We add the results of Hoshen & Malik (2019) and ours into the original recall-precision point sets and display them in Fig. 11, with khaki dot and red dot.

Previously, the best $(F_8, F_{1/8})$ pairs were got by Hoshen & Malik (2019) in MNIST, FASHION-MNIST, and we get slightly better scores on the both datasets. For the CIFAR-10 dataset, the precision of our model slightly underperform gan, but achieve better recall scores. Our recall score is also better than GLANN Hoshen & Malik (2019). The proposed model does not achieve better score than the highest one of GANs on CelebA dataset, due to imprecision of pre-trained autoencoder. If we expand the capacity of the autoencoder network, our model can get better scores. In particular, when adopting the GCGAN architecture Radford et al. (2016) as the decoder and its mirror as encoder, our model attains the best $(F_8, F_{1/8})$ score at $(0.807, 0.906)$. We draw this point in Fig. (11) as purple dot and the generated images is shown in Fig. 12.

The core problem of AE-OT is that if the autoencoder fails to approximate the manifold in the image space well, then the proposed method may not give a realistic result, just as the results of CelebA. But if the autoencoder approximates the original manifold well, our theory can guarantee to generate good results (proved by the FID and PRD scores of the expanded autoencoder and the images shown in Fig. 12).

C.7 Linear Interpolation in the latent space

Given any two images in the dataset, we can find the images between them by linear interpolation in the noise space because the one to one correspondence between μ mass centers in the noise space and the images in the dataset is provided by the proposed algorithm. For other generation models, though the interpolation can be done successfully in the noise space, they cannot find the correspondence from the noise space and the image space. The results of the linear interpolation are shown in Fig. 13.

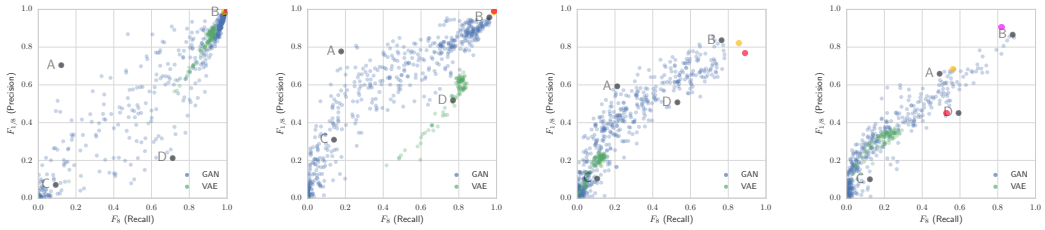

(a) MNIST (b) FASHION (c) CIFAR-10 (d) CelebA

Figure 11: The comparison of Precision-Recall pair in $(F_8, F_{1/8})$ in the 4 datasets. The khaki dots are the results of Hoshen & Malik (2019). The red dots are the results of the proposed method. The purple dot in the forth subfigure corresponds to the results of the architecture with two more convolutional layers.

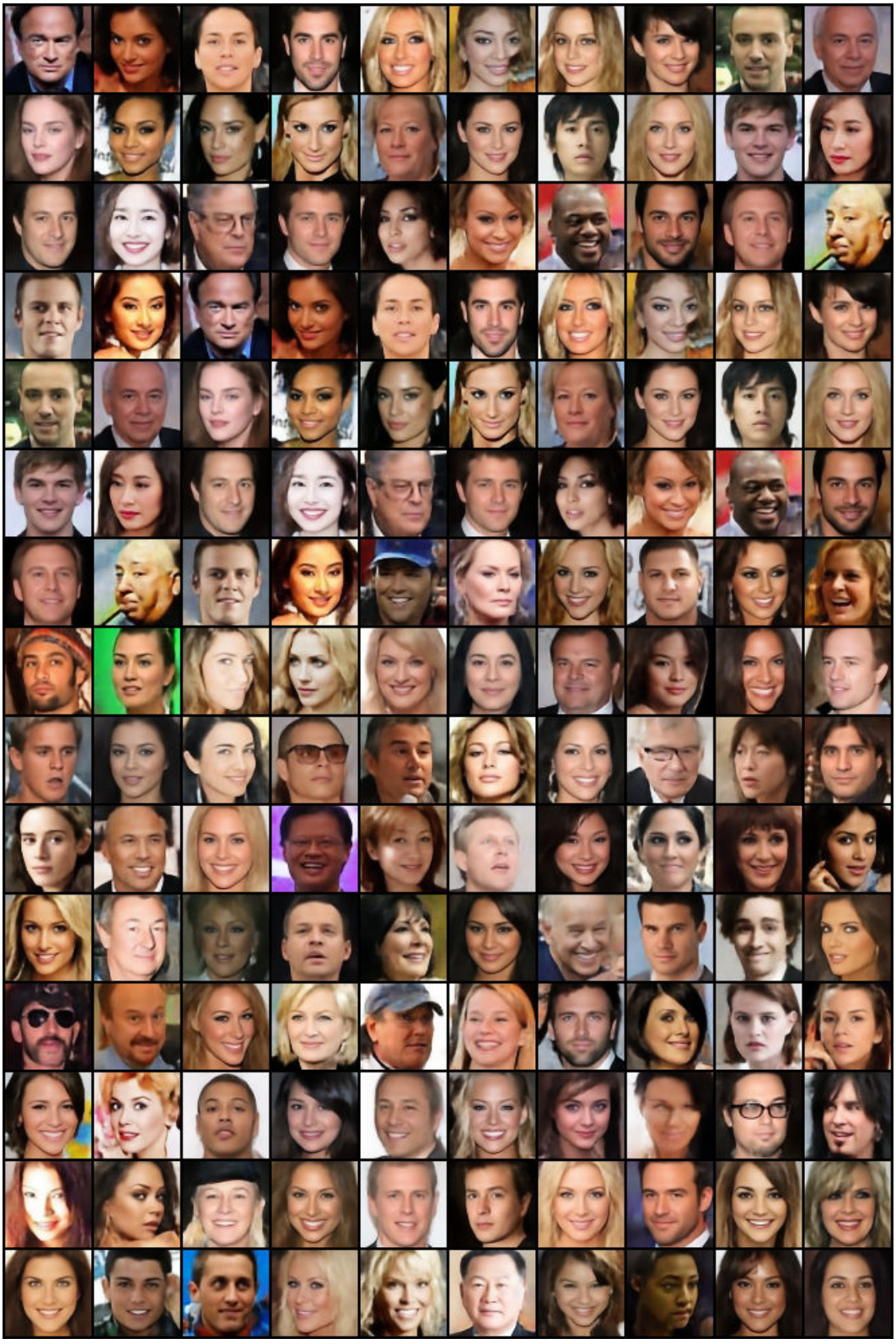

Figure 12: The generated human faces with the architecture originated from DCGAN Radford et al. (2016)

Figure 13: The linear interpolation between given two faces in the dataset.